20XX-01-XXXX

Quantitative Feedback Control of Air Path in Diesel-Dual-Fuel Engine

Withit Chatlatanagulchai and Nitirong Pongpanich
Faculty of Engineering, Kasetsart University

Shinapat Rhienprayoon and Krisada Wannatong
PTT Research and Technology Institute, PTT Public Company Limited

ABSTRACT

In this paper, we investigate a multivariable control of air path of a diesel-dual-fuel (DDF) engine. The engine is modified from a CI engine by injecting CNG in intake ports. The engine uses CNG as its primary fuel and diesel as its secondary fuel, mainly for initiation of combustion. The modification is economically attractive because CNG has lower price than diesel and the modification cost is minimal. However, for DDF engine, control of the air path becomes more difficult because the engine now has combined characteristics of the CI and the SI engines. The combined characteristics come from the fact that diesel is still directly injected into cylinders (CI engine) while CNG is injected at the intake ports (SI engine.) In pure CI engine, throttle is normally fully opened for maximum air intake, while EGR valve is actively actuated to obtain low emissions. In pure SI engine, however, throttle is an active actuator, driven by pedal. The air path control of the DDF engine, therefore, is a multivariable problem, where both throttle and EGR valve are actively actuated to obtain desired outputs. Two outputs that are of particular interest are mass air flow (MAF) and manifold air pressure (MAP). They are directly available from existing vehicle sensors and are good indicators of the air path characteristic. Their desired values are normally obtained as fixed maps during engine calibration. We formulate a control problem, having throttle and EGR valve openings as inputs and MAF and MAP as outputs. Because of high level of input-to-output interactions, a fully multivariable controller is preferred over the decentralized control. A multivariable control based on the quantitative feedback theory (QFT) is designed and implemented. The QFT-based controller is attractive because its robustness amount can be quantified. Control design plant model is allowed to have uncertainty within a boundary called plant template. For all uncertainty within a plant template, a controller and a prefilter are designed from loop shaping to enforce several frequency-domain specifications such as tracking, stability, disturbance and noise rejections, and control effort limitation. A 2KD-FTV Toyota CI engine is modified as a DDF engine and is installed in a test cell with an engine dynamometer. A system identification of the air path is performed to obtain a control design model. Both simulation and experimental results on the engine show the effectiveness of the proposed control system in tracking step changes of desired MAF and MAP.

INTRODUCTION

In countries that can produce its own natural gas, CNG may have lower price than diesel. CNG has long been used as an alternative fuel for the SI engine. With minor modification to the engine, CNG can be injected in the intake ports and be used fully in place of gasoline. This convenience comes from the fact that there exist spark

plugs to help ignite the CNG. In CI engine, however, the CNG cannot be used fully in place of diesel because the compression ratio is not high enough to ignite the CNG. To use CNG with CI engine, unless major engine modification is done, diesel is still needed in a smaller amount to initiate the combustion. CNG can be used as primary fuel and can be injected at the intake ports. The so-called diesel-dual-fuel (DDF) engine concept can reduce total fuel cost while still obtain good efficiency and performance of the CI engine.

The challenge comes from having two fuels in use at the same time. CNG is injected at the intake ports, which is mixed with fresh air before going into the combustion chamber. This SI engine-like behavior requires precise air/fuel ratio regulation. Diesel is also injected directly into the combustion chamber, where EGR amount must be carefully controlled.

While steady-state mappings can be performed during engine calibration, the engine suffers from poor performance during transients. During sudden load or speed changes, fresh air normally lags due to delays from turbocharger and compressible property of air. This emphasizes the necessity to have high-performance control system of the air path.

Existing literature on air path control of DDF engine is very limited. Ref. [1] presents an algorithm in choosing to actuate either throttle or EGR valve to regulate air/fuel ratio, while pumping loss is minimized. Ref. [2] adds the effect on adjusting the total fuel amount.

In CI engine, normally EGR valve and variable geometry turbine (VGT) are actuated to control MAF and MAP. Existing algorithms in use can be divided into three groups, according to type of the plant model used in control design.

The first group is designed based on two-by-two matrix, containing plant transfer functions. Existing algorithms are as follows: H_∞ mixed synthesis [3], two-degree-of-freedom H_∞ loop-shaping [4], gain-scheduling H_∞-based control [5], linear matrix inequality (LMI) control [6], linear quadratic Gaussian (LQG) [7], decentralized control [8], model predictive control [9].

The second group is designed based on linear or nonlinear state-space model. Existing algorithms are as follows: dynamic feedback linearization [10], backstepping control [11], sliding mode control [12], constructive Lyapunov control [13], output-feedback PID control [14], nonlinear model predictive control [15].

The third group, probably the least popular, is designed based on unknown plant model. Existing algorithm is fuzzy logic control [16].

In this paper, we present a control system based on quantitative feedback theory (QFT), originated around fifty years ago by I. Horowitz [17]. Although QFT was originated decades ago, its applications have just been accelerated in the late 80s and early 90s due to the advent of the QFT computer-aided-design (CAD) packages [18]-[20].

QFT design is performed on the Nichols chart. Three main steps are as follows. First, time-domain specifications are converted to frequency domain. Second, frequency-domain specifications are converted to bounds on the Nichols chart. Third, loop shaping is performed to shape the open-loop plot on the Nichols chart. After the open-loop plot is shaped to satisfy all specification bounds, time-domain specifications are met.

The authors are not aware of any existing literature that applies QFT to the air-path control. Some advantages over existing techniques mentioned above are as follows:

- QFT is designed on a set of plant model, called plant template, which contains all possible plants. The designer can specify any possible plant model variation, for example, different plant model for different speed and load. At the end, the resulting controller will ensure that all specifications are met for all plant variation.
- Various time-domain specifications can be set. They are tracking, disturbance and noise rejection, control effort limitation, and model matching.
- Specifications are converted to graphical bounds on the Nichols chart. Open-loop plot is shaped to satisfy all bounds. The designer directly sees the amount of over designs and can reduce them, resulting in the least-conservative controller.

A 2KD-FTV Toyota CI engine is modified as a DDF engine and is installed in a test cell with an engine dynamometer. A two-by-two transfer function matrix, relating throttle position sensor (TPS) readings and EGR valve opening to MAF and MAP, is found from black-box system identification. Multivariable QFT-based controller and prefilter are designed and tested in simulation and experiment. MAF and MAP can follow their set points closely. The air-path control system benefits from the advantages of the QFT technique mentioned above.

The paper is organized as follows. Next section presents system identification of the air path, followed by control system design section. Results are given in simulation results and experimental results sections. The paper is closed with conclusions, references, contact information, and acknowledgments.

AIR-PATH SYSTEM IDENTIFICATION

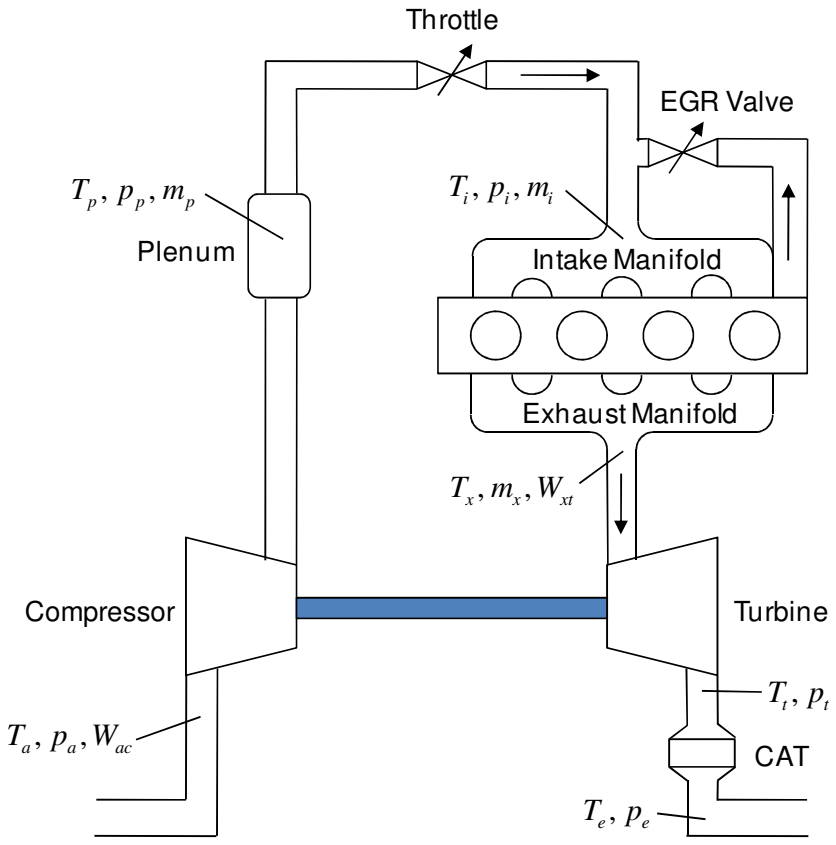

Figure 1: Air-path system of the DDF engine with measured signals.

Figure 1 depicts the air-path system in the 2KD-FTV Toyota engine, which is modified to run as DDF engine and is installed in our test cell with an engine dynamometer. The test cell management system is AVL PUMA, and data acquisition and control hardware is National Instruments.

Parameters in Figure 1 describe measurable quantities from the engine test bed. T, p, W, m are for temperature, pressure, mass flow rate, and mass, respectively. Subscripts a, c, p, i, x, t, e are for ambient, compressor, plenum, intake manifold, exhaust manifold, turbine, and exhaust pipe, respectively. Throttle and EGR valves are two actuators to control MAF and MAP, which are denoted by W_{ac} and p_i in Figure 1.

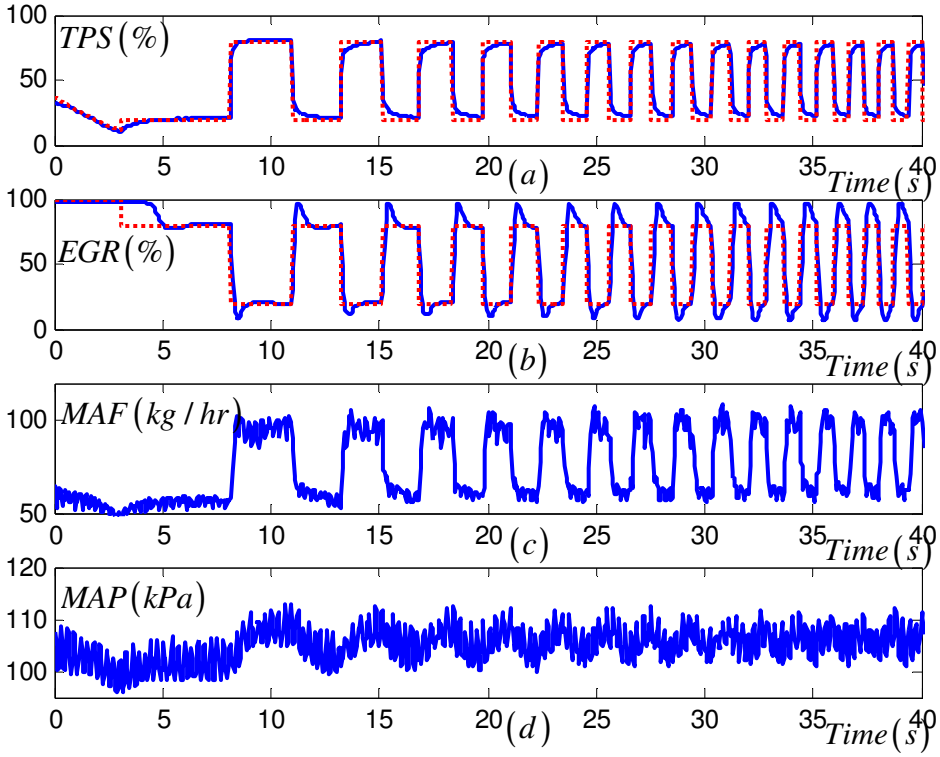

Figure 2: Validation data for system identification. Dash lines are reference values. Solid lines are actual values. (a) Throttle position sensor readings (in percent opening). (b) EGR valve opening (in percent opening). (c) Mass air flow (MAF). (d) Manifold absolute pressure (MAP).

Figure 2 contains measured signals of TPS, EGR, MAF, and MAP used in model validation. Dash lines are reference values, and solid lines are actual values. In finding the plant transfer function matrix relating inputs TPS and EGR to outputs MAP and MAF, three facts are used:

- Fixed maps, obtained during engine calibration, provide required values of TPS and EGR to obtain specific values of MAF and MAP. These values of TPS and EGR are used as feed-forward term in control system. Since the controller only handles deviations from the fixed maps, the plant transfer function matrix only relates the deviations of inputs to the deviations of outputs. Therefore, in finding the plant transfer function matrix, mean values of all signals are removed.
- EGR moves in the opposite direction to MAP and MAF, that is, increasing EGR results in decreasing MAP and MAF and vice versa. Therefore, transfer functions relating ΔEGR to ΔMAP and ΔMAF have non-minimum-phase zeros, which limit controller performance. Transfer functions from $-\Delta EGR$ to ΔMAP and ΔMAF are used instead to avoid the non-minimum-phase problem.

- In Figure 2(a) and (b), dash lines are reference values, while solid lines are actual values of TPS and EGR. We can only specify the reference values. The actual values are those obtained from well-tuned PID controllers that are used to control TPS and EGR positions. The transfer functions are computed from actual values.

The two-by-two plant transfer function matrix is found as

$$\begin{bmatrix} \Delta MAP \\ \Delta MAF \end{bmatrix} = \begin{bmatrix} p_{11} & p_{12} \\ p_{21} & p_{22} \end{bmatrix} \begin{bmatrix} \Delta TPS \\ -\Delta EGR \end{bmatrix} = \begin{bmatrix} \dfrac{0.101}{0.01192s+1} & \dfrac{0.2001}{2.165s+1} \\ \dfrac{0.1197}{0.001619s+1} & \dfrac{0.4157}{0.001s+1} \end{bmatrix} \begin{bmatrix} \Delta TPS \\ -\Delta EGR \end{bmatrix}. \quad (1)$$

p_{11} and p_{21} are found by closing EGR fully and allowing TPS to follow a frequency-varying square wave. p_{12} and p_{22} are found by opening TPS fully and allowing EGR to follow a frequency-varying square wave. After removing means from all signals, a Matlab function, $\langle ident \rangle$, is used to find the transfer functions. The model is validated using different set of data, shown in Figure 2. As shown in Figure 3, model outputs match actual outputs closely, indicating good accuracy of the model.

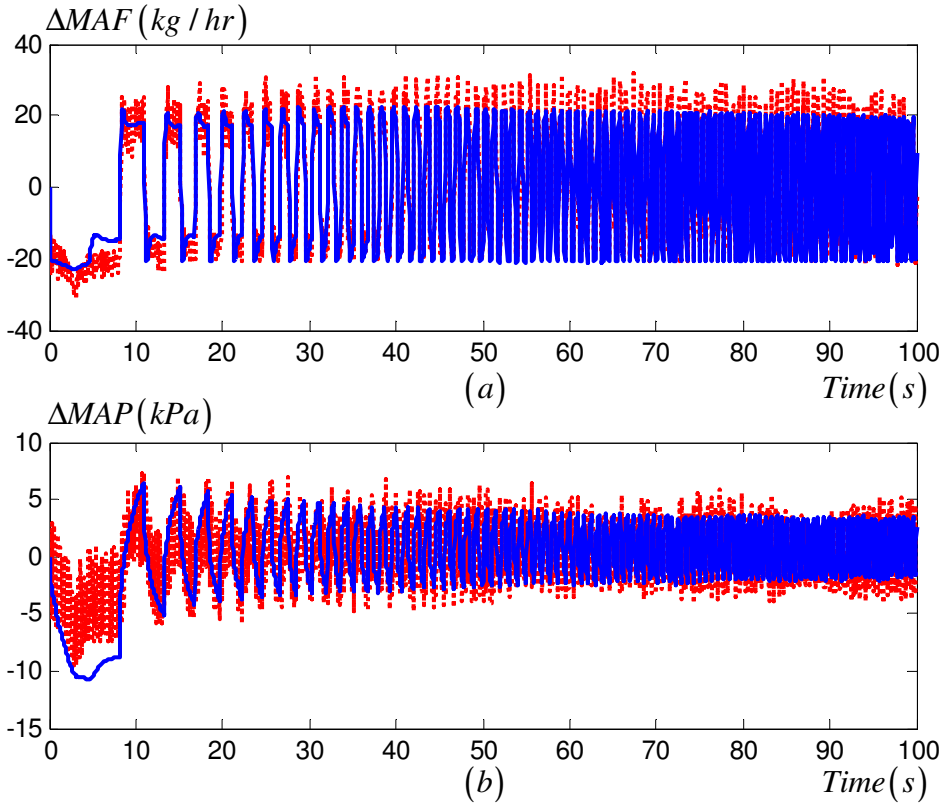

Figure 3: Model validation using a different set of data, shown in Figure 2. Dash lines are actual values. Solid lines are model values. (a) $\Delta MAF\,(kg/hr)$. (b) $\Delta MAP\,(kPa)$.

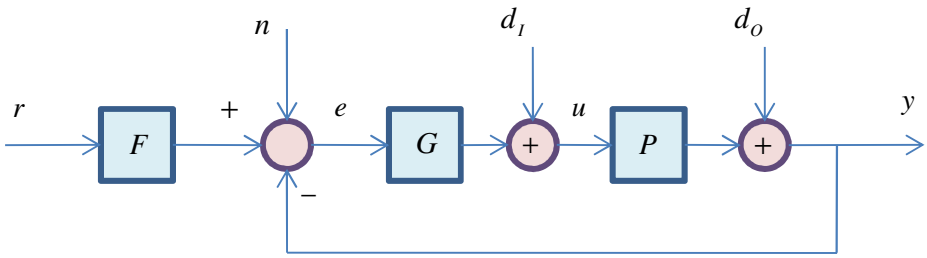

Figure 4: A two-degrees-of-freedom, multi-inputs-multi-outputs feedback system.

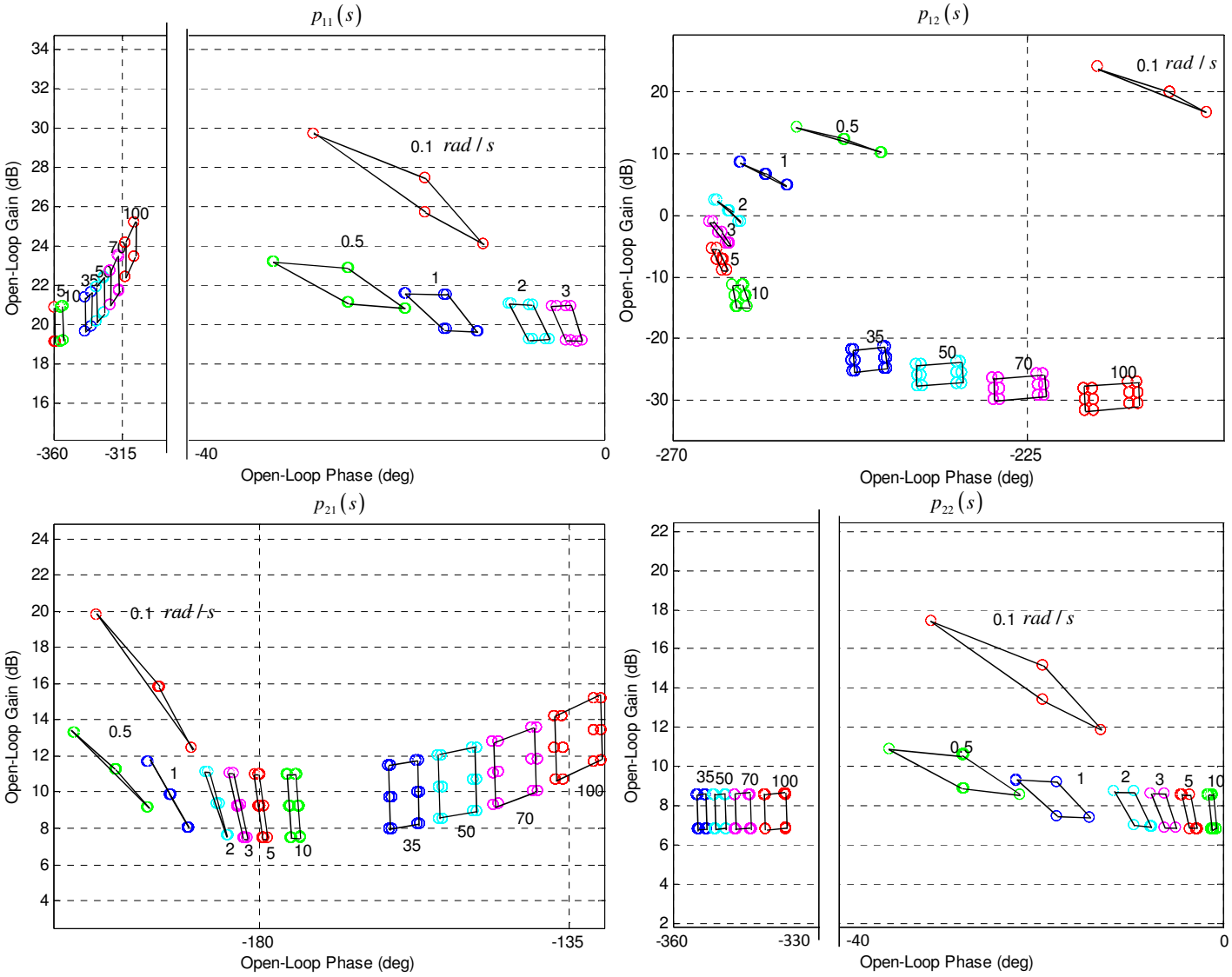

Figure 5: Plant templates on the Nichols chart at various frequencies. Top-left is p_{11}. Top-right is p_{12}. Bottom-left is p_{21}. Bottom-right is p_{22}.

CONTROL SYSTEM DESIGN

The control system is depicted in Figure 4, where n is signal noise, d_I is plant-input disturbance, d_O is plant-output disturbance, r is reference input, u is control input, y is plant output, P is two-by-two plant transfer function matrix $P=[p_{11}, p_{12}; p_{21}, p_{22}]$ with inverse $P^{-1}=[\pi_{11}, \pi_{12}; \pi_{21}, \pi_{22}]$. A prefilter and a controller $G=[g_1, 0; 0, g_2]$ are to be designed.

PLANT TEMPLATES

Adding 10% more uncertainties to each parameter in the plant model (1) and letting $s = j\omega$, plant templates at various frequencies can be plotted on the Nichols chart as shown in Figure 5. Instead of a single-point plant, the controller and the prefilter are designed to meet all specifications for all plant variations within the plant templates.

FREQUENCY-DOMAIN SPECIFICATIONS

In this section, we list various specifications for the controller and prefilter design. Only four specifications, which are plant-input and plant-output disturbance rejections, tracking, and stability, are included in our design. For model matching, noise rejection, and control effort limitation, the reader is referred to [21] for more details.

Plant-Input Disturbance Rejection

From Figure 4, the transfer function from plant-input disturbance to plant output is

$$T_{dI}=\begin{bmatrix} t_{dI11} & t_{dI12} \\ t_{dI21} & t_{dI22} \end{bmatrix}=(I+PG)^{-1}P. \tag{2}$$

Multiplying both sides of (2) by

$$\begin{bmatrix} 1 & 0 \\ \dfrac{-\pi_{21}}{\pi_{11}+g_1} & 1 \end{bmatrix} P^{-1}(I+PG)$$

and solving the resulting equations, we have

$$t_{dI11}=\frac{1-\pi_{12}t_{dI21}}{\pi_{11}+g_1}, t_{dI12}=\frac{-\pi_{12}t_{dI22}}{\pi_{11}+g_1}, t_{dI21}=\left(\frac{-\pi_{21}}{\pi_{11}+g_1}\right)/\left(\frac{-\pi_{21}\pi_{12}}{\pi_{11}+g_1}+\pi_{22}+g_2\right), t_{dI22}=1/\left(\frac{-\pi_{21}\pi_{12}}{\pi_{11}+g_1}+\pi_{22}+g_2\right).$$

Since we want to minimize the effect of the plant-input disturbance to the plant output, the specifications are given by $0\le|t_{dIij}|\le b_{dIij}; i, j=1, 2,$ where b_{dIij} are constants close to zeros.

Applying the specifications to the transfer function from plant-input disturbance to plant output, we have

$$0 \le \left| \frac{1 \pm |\pi_{12}| b_{dI21}}{\pi_{11} + g_1} \right| \le b_{dI11}, \tag{3}$$

$$0 \le \left| \frac{\pm |\pi_{12}| b_{dI22}}{\pi_{11} + g_1} \right| \le b_{dI12}, \tag{4}$$

$$0 \le \left| \left(\frac{-\pi_{21}}{\pi_{11} + g_1} \right) / \left(\frac{-\pi_{21}\pi_{12}}{\pi_{11} + g_1} + \pi_{22} + g_2 \right) \right| \le b_{dI21}, \tag{5}$$

$$0 \le 1 / \left| \left(\frac{-\pi_{21}\pi_{12}}{\pi_{11} + g_1} + \pi_{22} + g_2 \right) \right| \le b_{dI22}, \tag{6}$$

where t_{dI21} and t_{dI22} are replaced with their bounds.

Plant-Output Disturbance Rejection

From Figure 4, the transfer function from plant-output disturbance to plant output is

$$T_{dO} = \begin{bmatrix} t_{dO11} & t_{dO12} \\ t_{dO21} & t_{dO22} \end{bmatrix} = (I + PG)^{-1}.$$

With similar derivation to that of the plant-input disturbance rejection, t_{dOij} can be found as

$$t_{dO11} = \frac{\pi_{11} - \pi_{12} t_{dO21}}{\pi_{11} + g_1}, \; t_{dO12} = \frac{\pi_{12} - \pi_{12} t_{dO22}}{\pi_{11} + g_1}, \; t_{dO21} = \left(\frac{-\pi_{21}\pi_{11}}{\pi_{11} + g_1} + \pi_{21} \right) / \left(\frac{-\pi_{21}\pi_{12}}{\pi_{11} + g_1} + \pi_{22} + g_2 \right),$$
$$t_{dO22} = \left(\frac{-\pi_{21}\pi_{12}}{\pi_{11} + g_1} + \pi_{22} \right) / \left(\frac{-\pi_{21}\pi_{12}}{\pi_{11} + g_1} + \pi_{22} + g_2 \right).$$

The specifications are given by $0 \le \left| t_{dOij} \right| \le b_{dOij}; i, j = 1, 2,$ with b_{dOij} being constants close to zeros.

Applying the specifications to the transfer function from plant-output disturbance to plant output, we have

$$0 \le \left| \frac{|\pi_{11}| \pm |\pi_{12}| b_{dO21}}{\pi_{11} + g_1} \right| \le b_{dO11}, \tag{7}$$

$$0 \le \left| \frac{|\pi_{12}| \pm |\pi_{12}| b_{dO22}}{\pi_{11} + g_1} \right| \le b_{dO12}, \tag{8}$$

$$0 \le \left| \left(\frac{-\pi_{21}\pi_{11}}{\pi_{11} + g_1} + \pi_{21} \right) / \left(\frac{-\pi_{21}\pi_{12}}{\pi_{11} + g_1} + \pi_{22} + g_2 \right) \right| \le b_{dO21}, \tag{9}$$

$$0 \le \left| \left(\frac{-\pi_{21}\pi_{12}}{\pi_{11}+g_1} + \pi_{22} \right) / \left(\frac{-\pi_{21}\pi_{12}}{\pi_{11}+g_1} + \pi_{22} + g_2 \right) \right| \le b_{dO22}. \tag{10}$$

Tracking

From Figure 4, the transfer function from reference input to plant output is

$$T_r = \begin{bmatrix} t_{r11} & t_{r12} \\ t_{r21} & t_{r22} \end{bmatrix} = (I + PG)^{-1} PGF.$$

With similar derivation to that of the plant-input disturbance rejection, t_{rij} can be found as

$$t_{r11} = \frac{g_1 f_{11} - \pi_{12} t_{r21}}{\pi_{11} + g_1}, \; t_{r12} = \frac{g_1 f_{12} - \pi_{12} t_{r22}}{\pi_{11} + g_1}, \; t_{r21} = \left(\frac{-\pi_{21}}{\pi_{11} + g_1} (g_1 f_{11}) + g_2 f_{21} \right) / \left(\frac{-\pi_{21}}{\pi_{11} + g_1} \pi_{12} + \pi_{22} + g_2 \right),$$

$$t_{r22} = \left(\frac{-\pi_{21}}{\pi_{11} + g_1} (g_1 f_{12}) + g_2 f_{22} \right) / \left(\frac{-\pi_{21}}{\pi_{11} + g_1} \pi_{12} + \pi_{22} + g_2 \right).$$

The specifications are given by $a_{rij} \le \left| t_{rij} \right| \le b_{rij}; i, j = 1, 2,$ where a_{rij} and b_{rij} are lower and upper bounds, which can be constants close to ones or transfer functions with appropriate time responses.

Applying the specifications to the transfer function from reference input to plant output, we have

$$a_{r11} \le \left| \frac{|g_1 f_{11}| \pm |\pi_{12}| b_{r21}}{\pi_{11} + g_1} \right| \le b_{r11}, \tag{11}$$

$$a_{r12} \le \left| \frac{|g_1 f_{12}| \pm |\pi_{12}| b_{r22}}{\pi_{11} + g_1} \right| \le b_{r12}, \tag{12}$$

$$a_{r21} \le \left| \left(\frac{-\pi_{21}}{\pi_{11} + g_1} (g_1 f_{11}) + g_2 f_{21} \right) / \left(\frac{-\pi_{21}}{\pi_{11} + g_1} \pi_{12} + \pi_{22} + g_2 \right) \right| \le b_{r21}, \tag{13}$$

$$a_{r22} \le \left| \left(\frac{-\pi_{21}}{\pi_{11} + g_1} (g_1 f_{12}) + g_2 f_{22} \right) / \left(\frac{-\pi_{21}}{\pi_{11} + g_1} \pi_{12} + \pi_{22} + g_2 \right) \right| \le b_{r22}. \tag{14}$$

Stability

In an MIMO system, we say that the stability margin for channel k is $m_k(\omega)$ if $\left| 1 + L_k(j\omega) \right|^{-1} = m_k(\omega),$ where $L_k(s)$ is obtained from closing all the loops except for the k^{th} loop, where the loop is opened at the k^{th} input to the controller. In our case, we have

$$L_1 = \frac{g_1}{\pi_{11} - \dfrac{\pi_{21}\pi_{12}}{\pi_{22} + g_2}} = \frac{g_1\left(p_{11} + g_2 \det P\right)}{1 + p_{22} g_2}, \; L_2 = \frac{g_2}{\pi_{22} - \dfrac{\pi_{12}\pi_{21}}{\pi_{11} + g_1}} = \frac{g_2\left(p_{22} + g_1 \det P\right)}{1 + p_{11} g_1}.$$

The stability margin specifications are then given by

$$\left|1 + \frac{g_1\left(p_{11} + g_2 \det P\right)}{1 + p_{22} g_2}\right|^{-1} \le m_1(\omega), \tag{15}$$

$$\left|1 + \frac{g_2\left(p_{22} + g_1 \det P\right)}{1 + p_{11} g_1}\right|^{-1} \le m_2(\omega). \tag{16}$$

Because g_1 is to be designed first, (15) is converted to contain only g_1 by letting the magnitude of g_2 approach the two extreme values (zero and infinity.) The specification (15) becomes

$$\lim_{|g_2|\to\infty} |1 + L_1|^{-1} = |1 + g_1 / \pi_{11}|^{-1} \le m_1(\omega) \tag{17}$$

$$\lim_{|g_2|\to 0} |1 + L_1|^{-1} = |1 + g_1 p_{11}|^{-1} \le m_1(\omega). \tag{18}$$

SEQUENTIAL DESIGN PROCESS

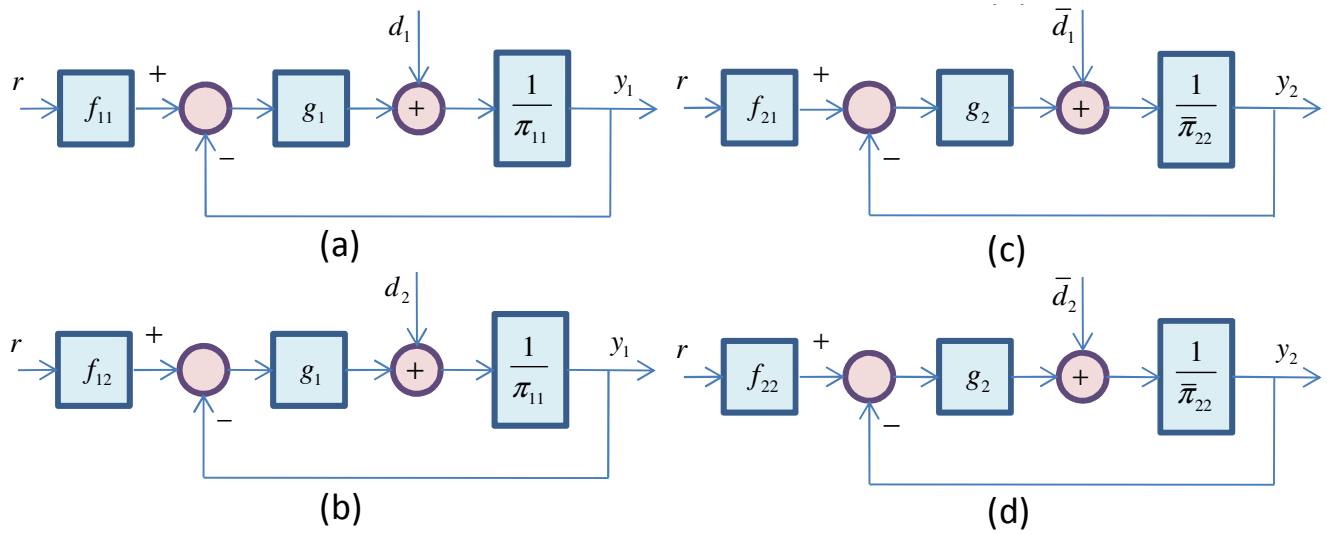

Figure 6: The MISO systems used to design controller and prefilter.

The MIMO design process can be transformed into the design of two sequential MISO systems. Consider the tracking specifications (11)-(14). Inequalities (11) and (12) are equivalent to the design of a MISO system in Figure 6(a) and (b) where $r(t) = \delta(t)$ and $|d_1| \le |\pi_{12}| b_{21}, |d_2| \le |\pi_{12}| b_{22}$ while inequalities (13) and (14) are equivalent to the design of a MISO system in Figure 6(c) and (d) where $r(t) = \delta(t)$,

$\bar{\pi}_{22} = -\pi_{21}\pi_{12} / (\pi_{11} + g_1) + \pi_{22}$, $\bar{d}_1 = -\pi_{21} g_1 f_{11} / (\pi_{11} + g_1)$, $\bar{d}_2 = -\pi_{21} g_1 f_{12} / (\pi_{11} + g_1)$. Therefore, the controllers g_1 and g_2 and the prefilters f_{11}, f_{12}, f_{21}, and f_{22} can be designed using QFT for their corresponding MISO system. The details of the QFT for MISO system can be found in [22].

For other specifications, which are input and output disturbances rejection, stability margins, noise rejection, control effort, and model matching, the design process can be formulated in a similar manner to that of the tracking specification.

LOOP SHAPING

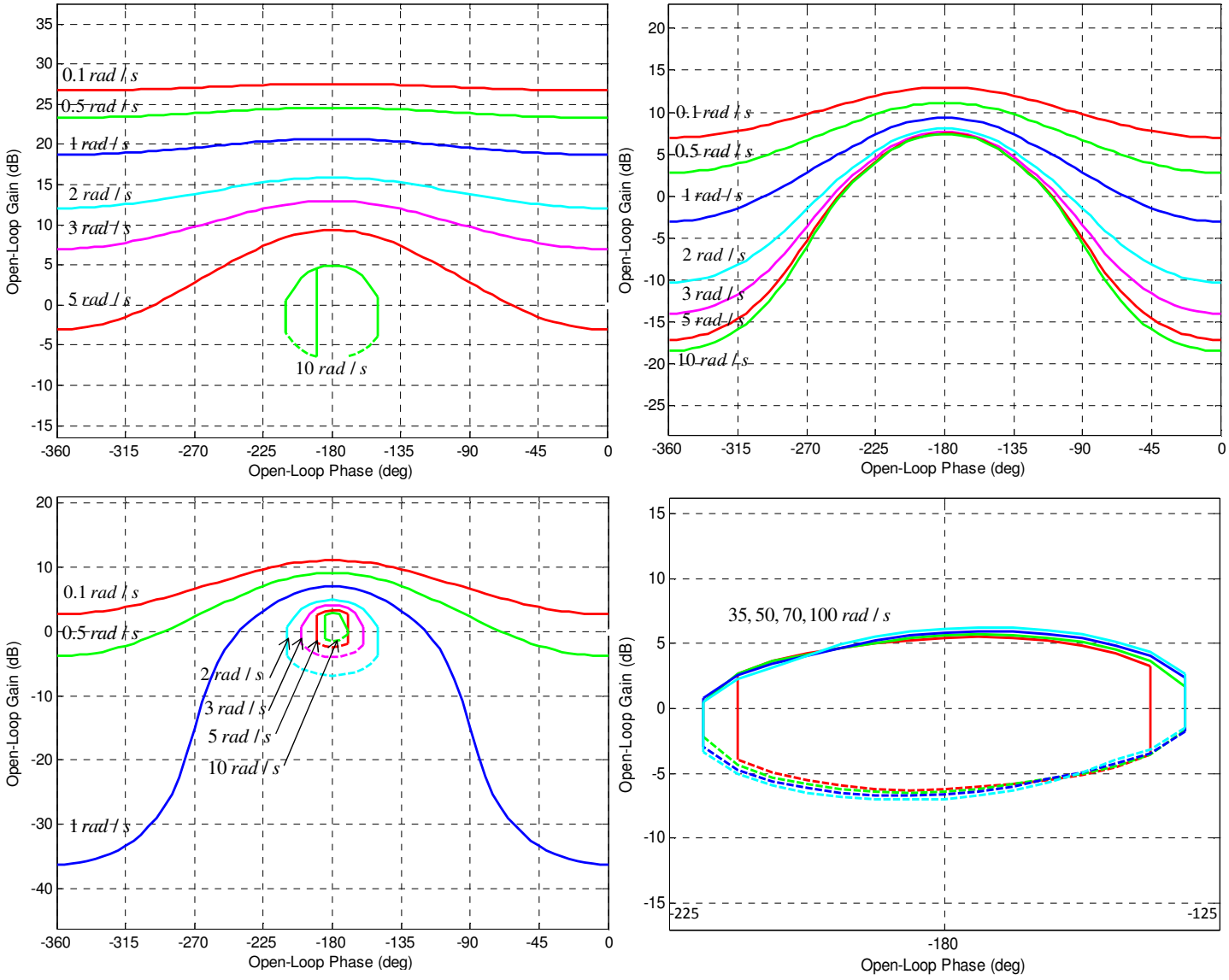

Figure 7: g_1 specifications: (top-left) tracking, (top-right) plant-input disturbance, (bottom-left) plant-output disturbance, (bottom-right) stability margins.

In this section, we design the controller $G = [g_1, 0; 0, g_2]$ and the prefilter $F = [f_{11}, f_{12}; f_{21}, f_{22}]$ of the closed-loop system in Figure 4. The plant is given by (1). For convenience, we let $f_{12} = f_{21} = 0$. The plant outputs, which are ΔMAP and ΔMAF are commanded to track two square waves ($r = [r_1; r_2]$) with 50% duty cycle, amplitude of 20, and period of 10 seconds. We also want the closed-loop system to be stable with a certain margin and to reject plant-input and plant-output disturbances. The same square waves as that used in tracking are used as disturbances ($d_I = [d_{I1}; d_{I2}]$ and $d_O = [d_{O1}; d_{O2}]$.) For convenience, the signals are assumed to be without noise ($n = [n_1; n_2] = [0; 0]$.) Using the sequential design process, g_1 and f_{11} are designed in step 1, and g_2 and f_{22} are designed in step 2.

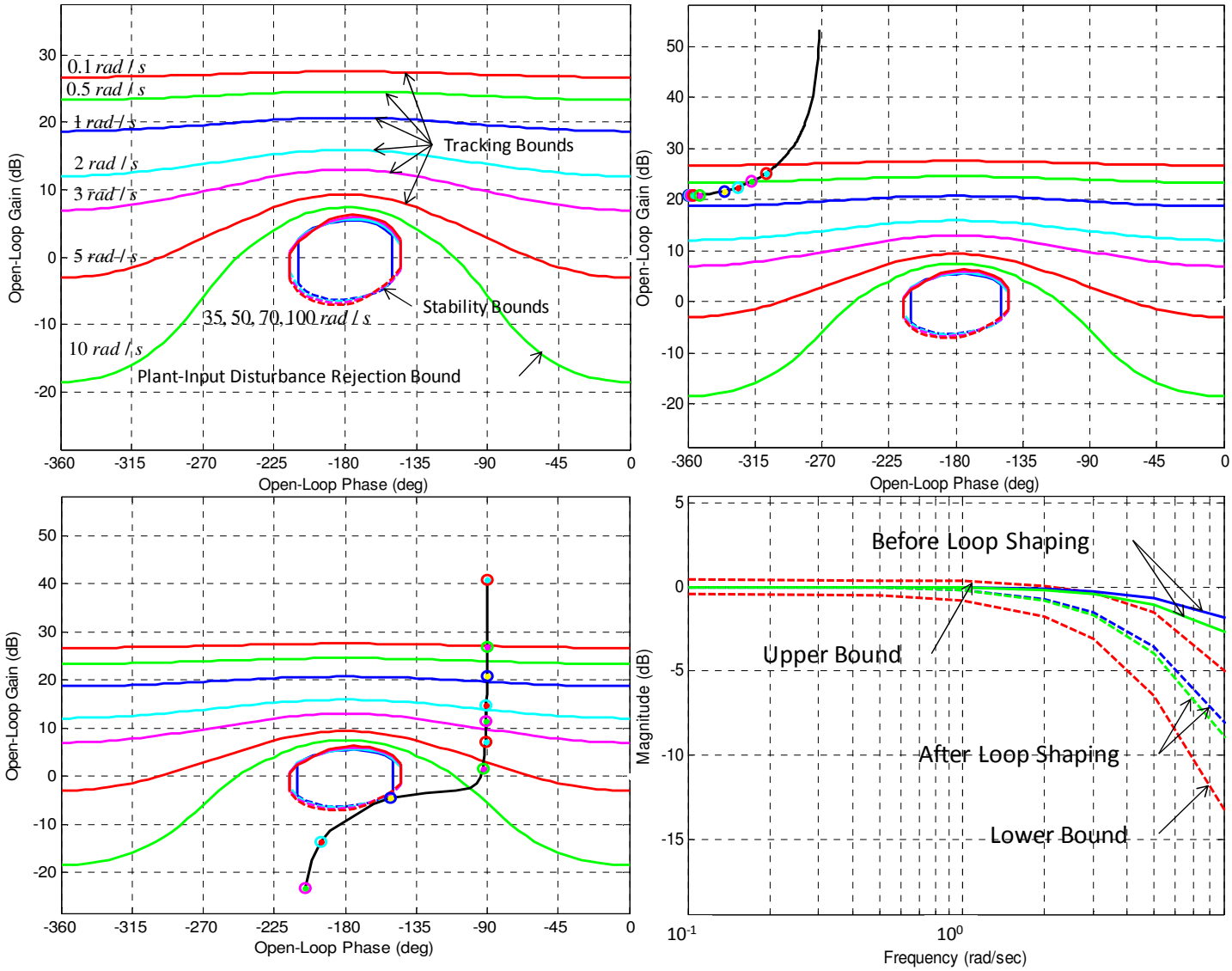

Figure 8: Loop shaping for g_1 and f_{11}. (Top-left) worst-case bounds. (Top-right) original open-loop shape. (Bottom-left) open-loop shape after loop shaping for g_1. (Bottom-right) loop shaping for f_{11}.

Step 1

We use the tracking specifications (11)-(12), letting $f_{12} = 0$ and a_{r11} and b_{r11} be two second-order transfer functions

$$a_{r11} = 0.95\frac{\omega_n^2}{s^2 + 2\zeta\omega_n s + \omega_n^2},\ b_{r11} = 1.05\frac{\omega_n^2}{s^2 + 2\zeta\omega_n s + \omega_n^2},$$

where $\zeta = 1, \omega_n = 5$ for a_{r11} and $\zeta = 1, \omega_n = 10$ for b_{r11}. To avoid interference from t_{12}, we let $b_{r12} = 0.1$ and $a_{r12} = 0.$ The resulting tracking bounds for frequencies $\omega = \{0.1, 0.5, 1, 2, 3, 5, 10\}$ rad/s are shown in Figure 7(top-left.) The resulting bounds for the plant-input and plant-output disturbance rejection specifications (3)-(4) and (7)-(8) where $b_{dI11} = b_{dI12} = b_{dO11} = b_{dO12} = 10$ are given in Figure 7(top-right) and Figure 7(bottom-left) respectively. The bounds for the stability margins specifications (17)-(18) with $m_1 = 6\ dB$ is given in Figure 7(bottom-right.) Note that, to ensure stability at high frequencies, we calculate the bounds for frequencies $\omega = \{35, 50, 70, 100\}$ rad/s.

The controller g_1 is loop-shaped to satisfy worst-case bounds, which are the strictest bounds among the four types of bounds in Figure 7, for each frequency. The worst-case bounds are shown in Figure 8(top-left.) Figure 8(top-right) contains open-loop shape before loop shaping ($g_1 = 1.$) Figure 8(bottom-left) shows the open-loop shape after loop shaping (g_1 is given below.) The prefilter f_{11} is loop-shaped to satisfy upper and lower tracking bounds as shown in Figure 8(bottom-right.)

The resulting g_1, comprising of a gain, an integrator, and a complex pole is given by

$$g_1 = \frac{1275.5901}{s\left(s^2 + 21.49s + 1276\right)}.$$

The resulting prefilter f_{11}, comprising of a gain and a real pole is given by

$$f_{11} = \frac{5.1369}{s + 5.137}.$$

Step 2

After the controller g_1 and the prefilter f_{11} are obtained, controller g_2 and prefilter f_{22} can be designed. Using the tracking specifications (13)-(14) and letting $f_{21} = 0$ and $b_{r22} = b_{r11}$, $a_{r22} = a_{r11}$, $b_{r21} = 0.5,$ and $a_{r21} = 0,$ we have the resulting tracking bounds as shown in Figure 9(top-left.) The resulting bounds for the plant-input and plant-output disturbance rejection specifications (5)-(6) and (9)-(10) where $b_{dI21} = b_{dI22} = b_{dO21} = b_{dO22} = 10$ are given in Figure 9(top-right) and Figure 9(bottom-left) respectively. The bounds for the stability margins specifications (15) and (16) with $m_2 = 6\ dB$ is given in Figure 9(bottom-right.)

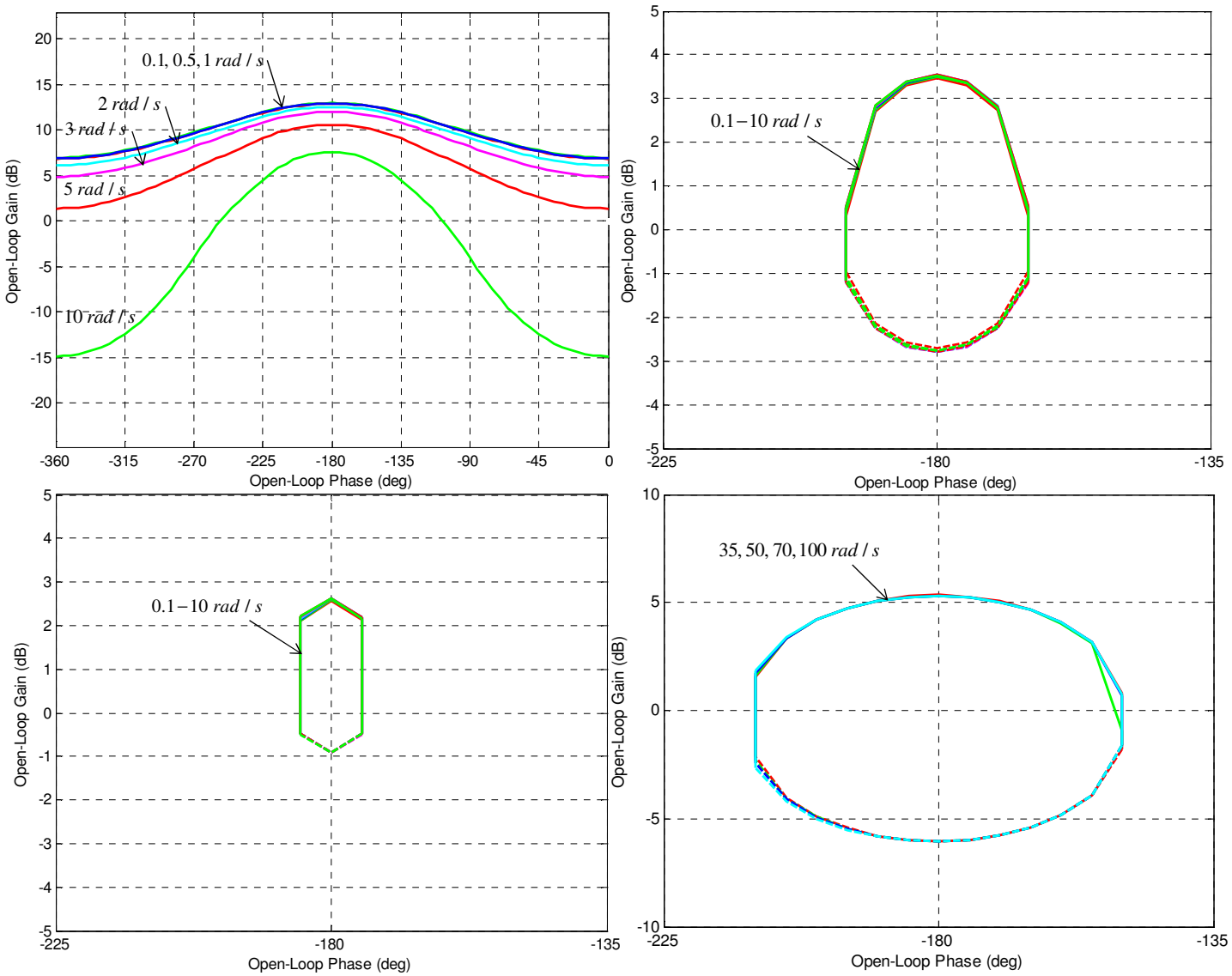

Figure 9: g_2 specifications: (top-left) tracking, (top-right) plant-input disturbance, (bottom-left) plant-output disturbance, (bottom-right) stability margins.

The controller g_2 and the prefilter f_{22} are loop-shaped to satisfy worst-case bounds, which are shown in Figure 10(top-left.) Figure 10(top-right) contains open-loop shape before loop shaping ($g_2 = 1.$) Figure 10(bottom-left) shows the open-loop shape after loop shaping (g_2 is given below.) The prefilter f_{22} is loop-shaped to satisfy upper and lower tracking bounds as shown in Figure 10(bottom-right.)

The resulting g_2, comprising of a gain, an integrator, and a complex pole is given by

$$g_2 = \frac{8207.3607}{s\left(s^2 + 21.93s + 2148\right)}.$$

The resulting prefilter f_{22}, comprising of a gain and a real pole is given by

$$f_{22} = \frac{5.4316}{s + 5.432}.$$

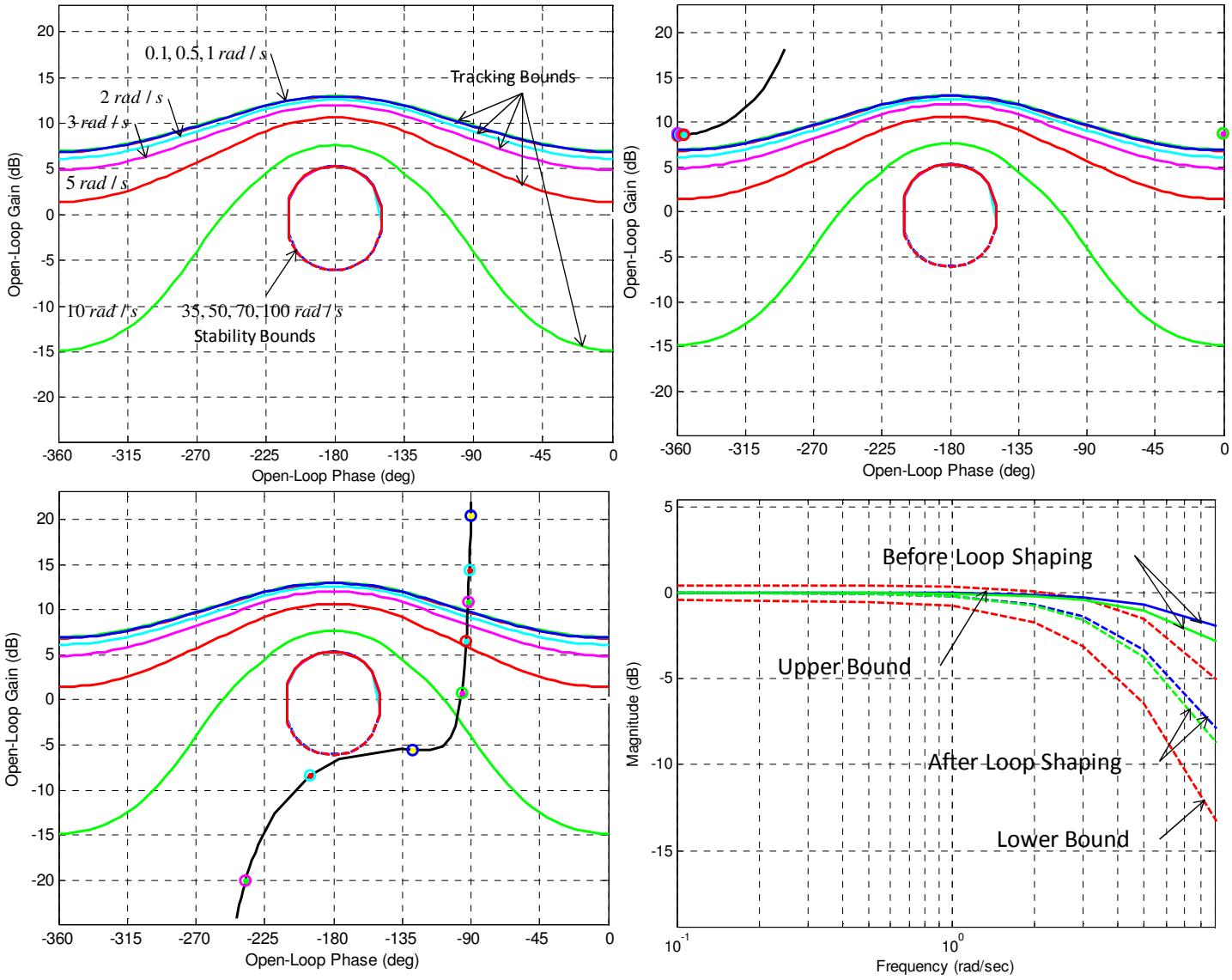

Figure 10: Loop shaping for g_2 and f_{22}. (Top-left) worst-case bounds. (Top-right) original open-loop shape. (Bottom-left) open-loop shape after loop shaping for g_2. (Bottom-right) loop shaping for f_{22}.

SIMULATION RESULTS

Consider the closed-loop system in Figure 4, in our case, $y = [\Delta MAP; \Delta MAF]$ and $u = [\Delta TPS; -\Delta EGR]$. r, d_I, and d_O are square waves with amplitude 20 units and period 10 seconds. P is the plant matrix given in (1). G and F are the controllers and the prefilters designed previously using QFT.

Assuming zero noise, the output y can be written as

$$y = (I + PG)^{-1} P\, d_I + (I + PG)^{-1} d_O + (I + PG)^{-1} PGF\, r,$$

$$\begin{bmatrix} \Delta MAP \\ \Delta MAF \end{bmatrix} = \begin{bmatrix} t_{dI11} & t_{dI12} \\ t_{dI21} & t_{dI22} \end{bmatrix} \begin{bmatrix} d_{I1} \\ d_{I2} \end{bmatrix} + \begin{bmatrix} t_{dO11} & t_{dO12} \\ t_{dO21} & t_{dO22} \end{bmatrix} \begin{bmatrix} d_{O1} \\ d_{O2} \end{bmatrix} + \begin{bmatrix} t_{r11} & t_{r12} \\ t_{r21} & t_{r22} \end{bmatrix} \begin{bmatrix} r_1 \\ r_2 \end{bmatrix}.$$

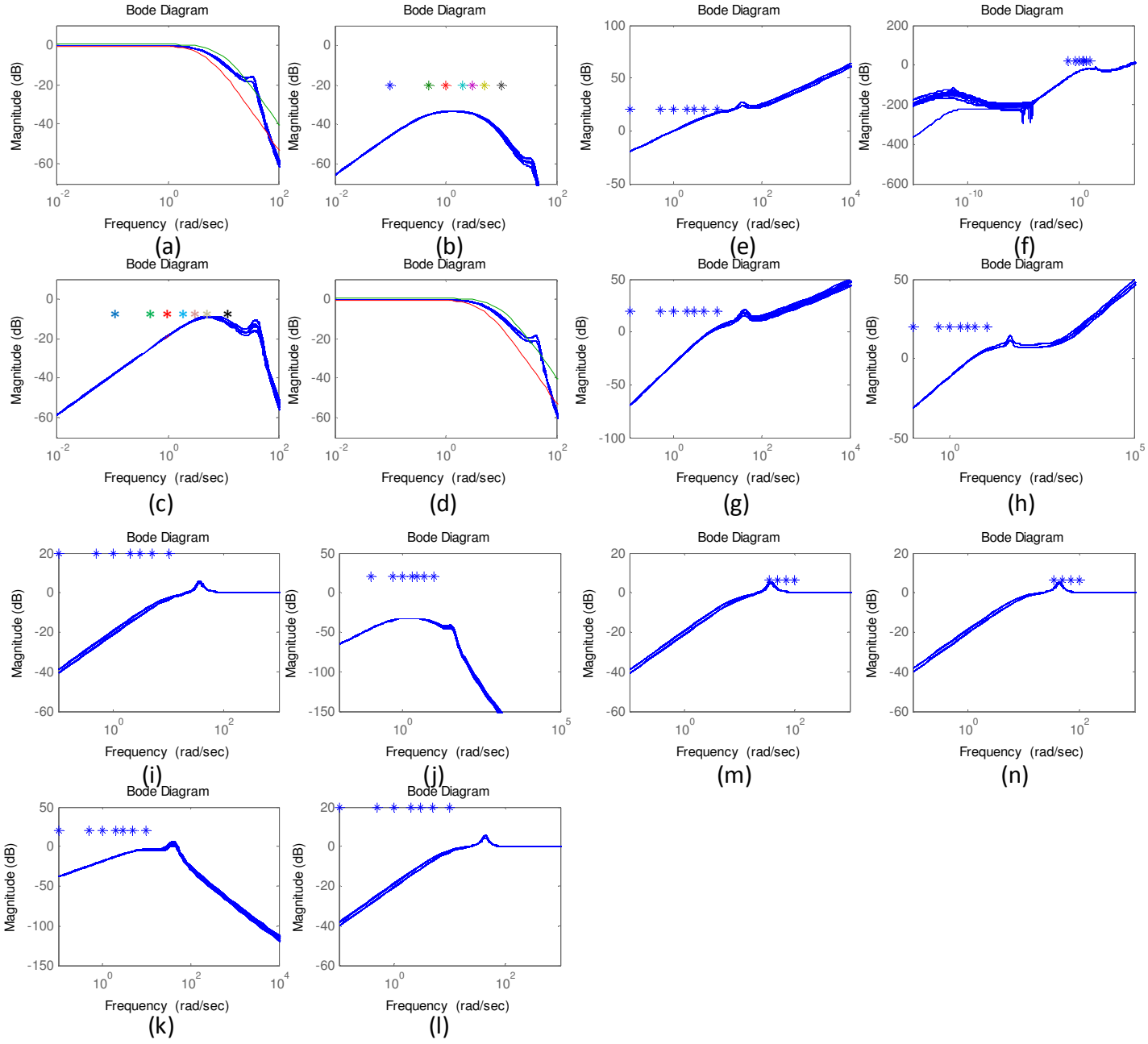

Figure 11: Frequency-domain simulation results. (a) t_{r11}. (b) t_{r12}. (c) t_{r21}. (d) t_{r22}. (e) t_{dI11}. (f) t_{dI12}. (g) t_{dI21}. (h) t_{dI22}. (i) t_{dO11}. (j) t_{dO12}. (k) t_{dO21}. (l) t_{dO22}. (m) $\left|1 + L_1\right|^{-1}$. (n) $\left|1 + L_2\right|^{-1}$.

The closed-loop frequency-domain simulation results are given in Figure 11, where the asterisks mark the upper bounds with the exception of those in Figure 11(a) and (d), where two solid lines mark $a_{r11}, b_{r11}, a_{r22},$ and b_{r22}.

One solid line represents an output of one plant case or one point on the plant template. We can see from Figure 11 that all frequency-domain specifications are met for all plant variations.

The time-domain simulation results are given in Figure 12. From Figure 12(e) and (f), both outputs are able to track the desired square wave well and within the specified lower and upper bounds for all plant variations. From Figure 12(g)-(j), both outputs can attenuate the square-wave disturbances very well.

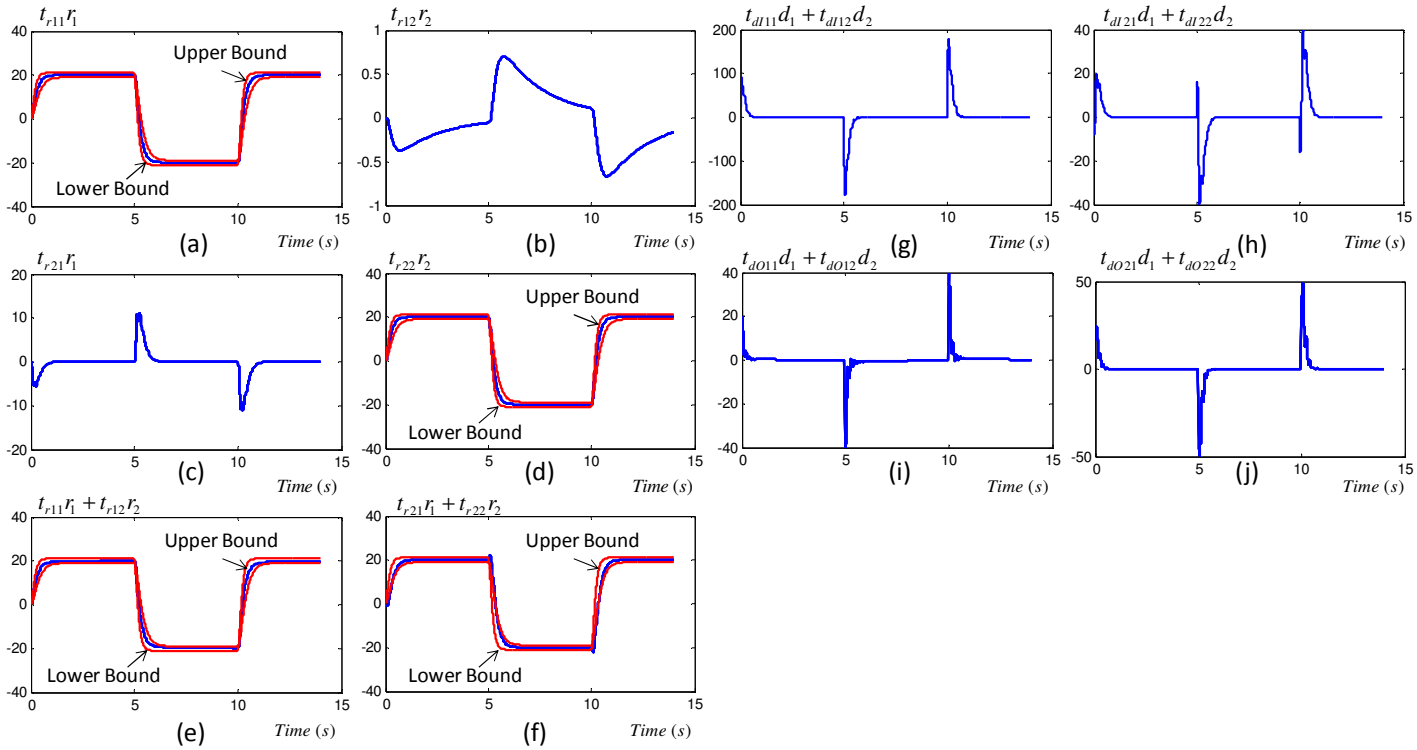

Figure 12: Time-domain simulation results. (a)-(f) Plant outputs from square-wave reference inputs. (g)-(h) Plant outputs from square-wave plant-input disturbances. (i)-(j) Plant outputs from square-wave plant-output disturbances.

EXPERIMENTAL RESULTS

We implemented the designed control system with a 2KD-FTV Toyota engine, mounted on a test bed with an engine dynamometer. Figure 13 contains block diagram of the closed-loop system used for implementation.

Two fixed maps, obtained off-line during engine calibration, determine desired MAP and MAF from engine speed and load. These desired MAP and MAF values are passed to other two fixed maps, again, obtained off-line during engine calibration, to determine nominal desired throttle and EGR valve positions. These values are used as feed-forward terms.

The designed QFT controller and prefilter are used to generate ΔTPS and $-\Delta EGR$ that, after sign conversion, are added to the feed-forward terms to become desired TPS and EGR valve positions.

Two PID controllers are used to control throttle and EGR valve to follow their desired positions.

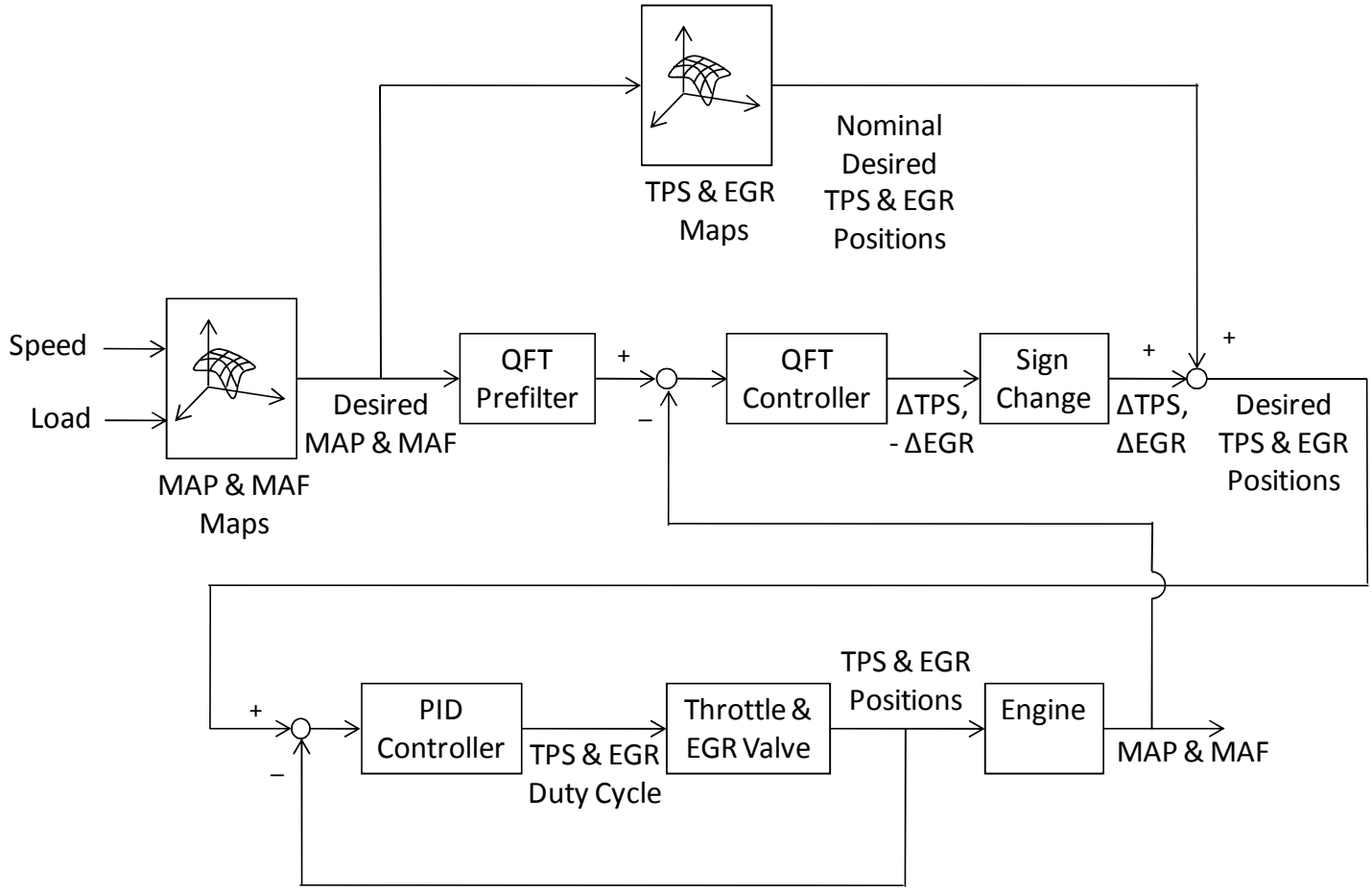

Figure 13: Implementation closed-loop system.

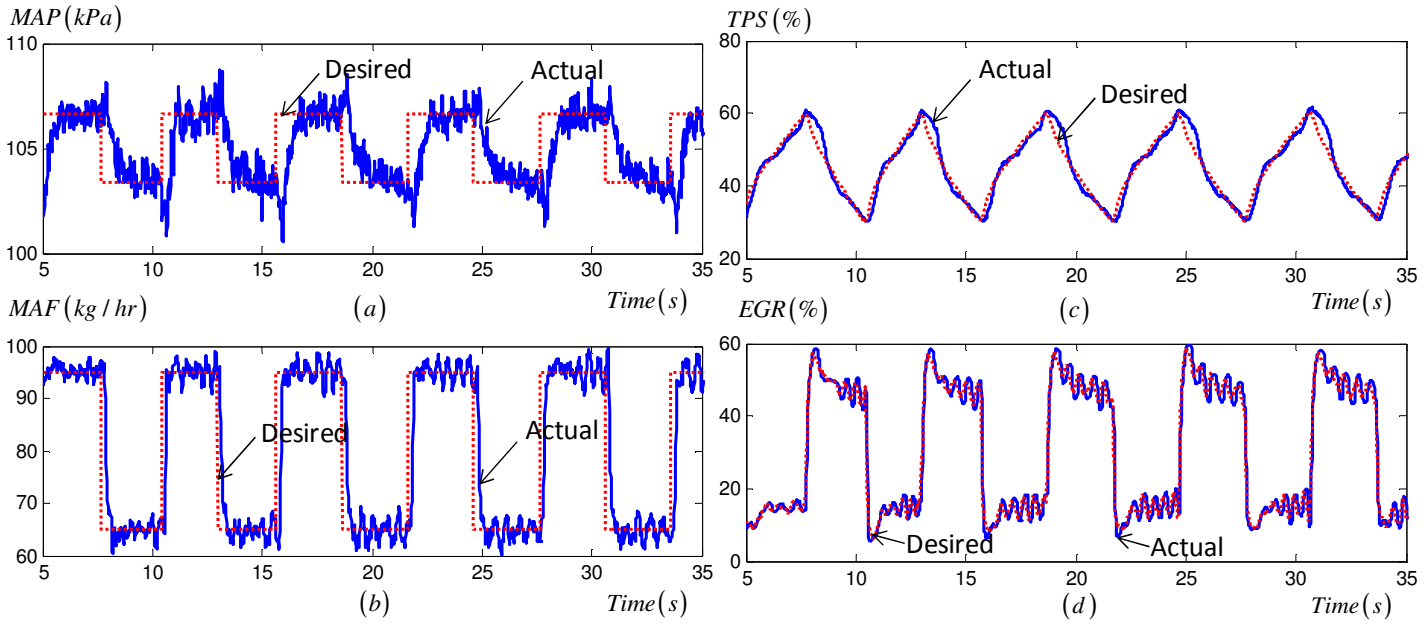

Figure 14: Experimental results. (a) MAP. (b) MAF. (c) TPS. (d) EGR.

Figure 14 shows experimental results. The actual MAP and MAF follow their desired values quite well as can be seen from Figure 14(a) and (b). Figure 14(c) and (d) contain desired and actual values of throttle and EGR valve positions.

CONCLUSIONS

Multivariable QFT-based control system is designed and implemented with the air path of the DDF engine. Throttle and EGR valves are actuated simultaneously to regulate MAP and MAF to their desired values. There are two significances of the results:

- In our awareness, this is one of the earliest works to apply QFT to air-path control problem, which brings several advantages such as the handling of all plant variations and the ability to specify various specifications and to obtain the least-conservative controller.
- Two features, regarding our modeling, are removal of signal means and switch the sign of the EGR valve position. Both result in simple-but-accurate first-order plant transfer functions, which are stable and have minimum phase.

However, there are two areas of our work that can be improved further:

- Our plant model uses actual TPS and EGR valve position signals as plant inputs. However, the controller only gives out the desired TPS and EGR values. We rely on two PID controllers to make the actual and desired values match closely as can be seen in Figure 14(c) and (d). Instead of the actual position signals, one can instead use the PWM duty cycles, which drive the throttle and EGR valve, as the plant inputs.
- In our humble opinion, multivariable control design has always been the QFT's weakness. The sequential design process, used in our work, is taken directly from [23]. One can investigate other multivariable techniques such as dynamical decoupling [24] or decentralized control based on input-output interactions [25].
- MAP and MAF signals measured from the real engine are contaminated by noise. We use them without filtering. One may try to filter the signals before performing system identification and during control system implementation. We find that the dominant noise frequencies are twice the engine speed because the intake valves are opened twice per one engine revolution.

REFERENCES

[1] Chatlatanagulchai, W., Yaovaja, K., Rhienprayoon, S., and Wannatong, K., "Air-Fuel Ratio Regulation with Optimum Throttle Opening in Diesel-Dual-Fuel Engine," to be presented at 2010 SAE International Conference on Powertrains, Fuels, and Lubricants, Brazil, May 5-7, 2010.

[2] Chatlatanagulchai, W., Yaovaja, K., Rhienprayoon, S., and Wannatong, K., "Air/Fuel Ratio Control in Diesel-Dual-Fuel Engine by Varying Throttle, EGR Valve, and Total Fuel," submitted to 2010 SAE Conference on Powertrains, Fuels, and Lubricants, San Diego, USA, October 25-27, 2010.

[3] Alfieri, E., Amstutz, A., and Guzzella, L., "Gain-Scheduled Model-Based Feedback Control of the Air/Fuel Ratio in Diesel Engines," *Control Engineering Practice* **17**:1417-1425, 2009.

[4] Jung, M., "Mean-Value Modelling and Robust Control of the Airpath of a Turbocharged Diesel Engine," Ph.D. thesis, Sidney Sussex College, Department of Engineering, University of Cambridge, Cambridge, 2003.

[5] Wei, X. and del Re, L., "Gain Scheduled H_∞ Control for Air Path Systems of Diesel Engines Using LPV Techniques," *IEEE Transactions on Control Systems Technology* **15**(3):406-415, 2007.

[6] Bengea, S., DeCarlo, R., Corless, M., and Rizzoni, G., "A Polytopic System Approach for the Hybrid Control of a Diesel Engine Using VGT/EGR," *Journal of Dynamic Systems, Measurement, and Control* **127**:13-21, 2005.

[7] Stefanopoulou, A. G., Kolmanovsky, I., and Freudenberg, J. S., "Control of Variable Geometry Turbocharged Diesel Engines for Reduced Emissions," *IEEE Transactions on Control Systems Technology* **8**(4):733-745, 2000.

[8] van Nieuwstadt, M. J., Kolmanovsky, I. V., Moraal, P. E., Stefanopoulou, A., and Jankovic, M., "EGR-VGT Control Schemes: Experimental Comparison for a High-Speed Diesel Engine," *IEEE Control Systems Magazine* 63-79, June 2000.

[9] Ferreau, H. J., Ortner, P., Langthaler, P., del Re, L., and Diehl, M., "Predictive Control of a Real-World Diesel Engine Using an Extended Online Active Set Strategy," *Annual Reviews in Control* **31**:293-301, 2007.

[10] Plianos, A., Achir, A., Stobart, R., Langlois, N., and Chafouk, H., "Dynamic Feedback Linearization Based Control Synthesis of the Turbocharged Diesel Engine," presented at the American Control Conference 2007, USA, July 11-13, 2007.

[11] Egardt, B., "Backstepping Control with Integral Action Applied to Air-to-Fuel Ratio Control for a Turbocharged Diesel Engine," presented at SAE World Congress and Exhibition 2002, USA.

[12] Utkin, V. I., Chang, H.-C., Kolmanovsky, I., and Cook, J. A., "Sliding Mode Control for Variable Geometry Turbocharged Diesel Engines," presented at 2000 American Control Conference, USA, June 2000.

[13] Jankovic, M., Jankovic, M., and Kolmanovsky, I., "Constructive Lyapunov Control Design for Turbocharged Diesel Engines," *IEEE Transactions on Control Systems Technology* **8**(2):288-299, 2000.

[14] Chauvin, J., Corde, G., Petit, N., and Rouchon, P., "Motion Planning for Experimental Airpath Control of a Diesel Homogeneous Charge-Compression Ignition Engine," *Control Engineering Practice* **16**, 2008.

[15] Herceg, M., Raff, T., Findeisen, R., and Allgower, F., "Nonlinear Model Predictive Control of a Turbocharged Diesel Engine," presented at 2006 International Conference on Control Applications, Germany, October 4-6, 2006.

[16] Shamdani, A. H., Shamekhi, A. H., and Ziabasharhagh, M., "Air Intake Modelling with Fuzzy AFR Control of a Turbocharged Diesel Engine," *Int. J. Vehicle Systems Modelling and Testing* **3**(1/2), 2008.

[17] Horowitz, I., "Fundamental Theory of Linear Feedback Control Systems," *Trans. IRE on Auto. Control* **AC-4**, 1959.

[18] Borghesani, C., "Computer Aided-Design of Robust Control Systems Using the Quantitative Feedback Theory," M.S. thesis, Mechanical Engineering Department, University of Massachusetts, Amherst, MA, 1993.

[19] Sating, R. R., "Development of an Analog MIMO Quantitative Feedback Theory (QFT) CAD Package," M.S. thesis, Graduate School of Engineering, Air Force Institute of Technology, Wright Patterson AFB, OH, 1992.

[20] Houpis, C. H. and Lamont, G., Digital Control Systems: Theory, Hardware, Software, McGraw-Hill, NY, 2nd Ed., 1992.

[21] Chatlatanagulchai, W., Srinangyam, C., and Siwakosit, W., "Trajectory Control of a Two-Link Robot Manipulator Carrying Uncertain Payload Using Quantitative Feedback Theory," *Journal of Research in Engineering and Technology* **5**(1):45-71, 2008.

[22] Chatlatanagulchai, W., Inseemeesak, B., and Siwakosit, W., "Quantitative Feedback Control of a Pendulum with Uncertain Payload," *Journal of Research in Engineering and Technology* **4**(4):347-367, 2007.

[23] Yaniv, O., Quantitative Feedback Design of Linear and Nonlinear Control Systems, Kluwer, Boston, 1999.

[24] Goodwin, G. C., Graebe, S. F., and Salgado, M. E., Control System Design, Prentice Hall, 2000.

[25] Skogestad, S. and Postlethwaite, I., Multivariable Feedback Control: Analysis and Design, Wiley, 2005.

CONTACT INFORMATION

Contact Withit Chatlatanagulchai at mailing address:

Department of Mechanical Engineering
Faculty of Engineering
Kasetsart University
50 Phaholyothin Road,
Bangkok 10900, Thailand

or email address: fengwtc@ku.ac.th

ACKNOWLEDGMENTS

Thanks are due to Kittipong Yaovaja for setting up the experimental hardware and collecting data for the system identification and Craig Borghesani and Terasoft for their evaluation copy of the QFT toolbox.